International Journal of Heat and Mass Transfer 241 (2025) 126749

Contents lists available at ScienceDirect

International Journal of Heat and Mass Transfer

journal homepage: www.elsevier.com/locate/ijhmt

Thermal characteristics of a medium- and high-temperature latent heat storage system under various operating conditions

Lei Zhang, Kelang Jin, Laiquan Lv, Shengyao Huang, Xue Xue, Xiang Liu, Hao Zhou *

Zhejiang University, Institute for Thermal Power Engineering, State Key Laboratory of Clean Energy Utilization, Hangzhou, 310027, PR China

ARTICLE INFO

Keywords:
Latent heat storage system
Phase change material
Visualize
Graded heating

ABSTRACT

Thermal energy storage units effectively address the spatiotemporal mismatch between energy production and demand. However, research on medium- and high-temperature latent thermal energy storage systems remains relatively scarce. This paper presents a small-scale, single-tube setup employing a spiral finned tube as the heat exchanger, leveraging its large surface area and capacity for natural convection. In the experiment, heat transfer oil, heated to a specific temperature in the boiler, enters the latent heat storage unit, exchanging heat with the phase-change material through the tube and spiral fins. The effects of heat transfer fluid flow rate and direction on the system's heat transfer performance were investigated by varying the oil's volumetric flow rate and inlet position. The underlying principles governing heat exchange are also discussed. Furthermore, a graded heat storage experiment was conducted, comparing the instantaneous power of the heat transfer oil with that of isothermal heat storage, revealing a potential method for power smoothing. A novel feature of the rig is the installation of a visualization window on one side, allowing for observation of the salt's state during both charging and discharging processes. The results show that the setup can store 5.5 MJ of energy in 33.35 kg of phase change material within 1.5 h. Increasing the heat transfer oil volumetric flow rate from 19.8 L/min to 33 L/min reduced the charging time by 33.2% and improved charging efficiency from 66.2% to 80.7%. During discharging, the solidification of PCM near the finned tube increased thermal resistance, resulting in a 36.1% reduction in discharging time, but only a slight increase in discharging efficiency from 65.7% to 69.9%. Experiments with varying inlet positions indicated that, at a flow rate of 33 L/min, charging should be initiated from the top of the heat exchange unit, while discharging should begin from the bottom. The graded heating process achieved a stabilized average power of approximately 1.234 kW during the charging process, significantly reducing the power fluctuation.

1. Introduction

As per the BP Energy Outlook 2023 report, the persistent increase in carbon emissions and increasing frequency of extreme weather events have more clearly demonstrated the importance of transitioning to a net-zero emissions future than ever before [1]. The report "Global Renewables Outlook: Energy Transformation 2050″ suggests that by 2050, the world should reduce its energy-related CO_2 emissions by 70% through renewable energy and improved energy efficiency [2]. However, renewable energy has technical limitations, including uneven power output, low economic feasibility, and instability [3], making it difficult to replace traditional energy sources on a large scale. Thermal Energy Storage (TES) technology could mitigate the temporal and spatial mismatch between the generation and consumption of energy [4], thereby strengthening the reliability of systems [5].

TES technology primarily consists of three classes: Sensible Heat Storage (SHS), Latent Heat Storage (LHS), and Thermochemical Heat Storage (TCHS) [6]. Compared with SHS, LHS boasts a higher energy density, and compared with TCHS, it exhibits excellent repeatability and controllability. Thus, it's currently considered one of the most promising TES technologies. Nevertheless, the poor thermal conductivity of Phase Change Materials (PCMs) significantly restricts the performance of LHS in both charging and discharging. And it seriously impedes their application in rapid charging and discharging scenarios [7]. In addition, TES technology can be divided into long-term storage and short-term storage according to the time of energy storage. At present, most of the research focuses on short-term storage, among which the research on adding nano-materials into phase change materials is the most, but it will lead

* Corresponding author.
E-mail address: zhouhao@zju.edu.cn (H. Zhou).

https://doi.org/10.1016/j.ijheatmasstransfer.2025.126749
Received 8 November 2024; Received in revised form 8 January 2025; Accepted 20 January 2025
Available online 27 January 2025

to the long-term recycling of phase change materials. A et al. discussed the use of additives in sugar alcohols and sodium acetate trihydrate, as well as the use change in a new type of phase change material capable of solid-solid phase change, and showed the promising characteristics of long-term heat storage materials [8].

To date, researchers have tackled this issue using four primary approaches. Firstly, the simplest and most effective approach is to increase the heat transfer area, which includes traditional methods that are easy to fabricate and cost-effective, such as longitudinal fins [9], annular fins [10], and helical fins [11]. Moreover, optimization methods tailored to specific fins are also included, such as using different diameters of annular fins at varying heights [12], perforated fins [13], and serrated fins [14]. For example, Abdullah et al. conducted a study on annular fins, using numerical simulations to optimize the number and size of fins, and it was found that more and longer fins significantly increased the melting rate of PCM [15]. Innovative structural and topological optimization schemes have been proposed, such as tree-shaped fins, snowflake fins, and pins fins [16]. Nidhal et al. made a major innovation in fins by using circular Y-type fins for the evaluation of heat transfer effect and also carried out an in-depth simulation of several parameters of the fins with the best heat transfer effect at an angle of 22.5° [17]. Notably, research by Shukla et al. has shown that as the number of branches on tree-shaped fins, the valid heat transfer area also increases. It resulted in a substantial enhancement in the thermodynamic efficiency of the system [18]. Zhang et al. have innovatively designed snowflake fins inspired by natural snowflakes, and experimental results have demonstrated that compared with traditional vertical fin configurations, the snowflake fin can reduce overall melting time by 32.23% and solidification time by 51.81% [19]. Chen et al. first used a topology optimization method to obtain a new fin, using a dual-objective function to derive a minimum field synergy angle at a ratio of 0.6:0.4 for the maximum average temperature to the minimum temperature difference, and the performance of the system was further improved [20]. The second approach involves enhancing PCM's conductivity through foam structures or enhancers. Zhang et al. conducted both experimental and numerical studies to investigate the performance of shell and tube devices featuring nickel foam embedded in nitrate, which demonstrated that the metal foam enhances the effective conductivity of solid PCM but attenuates the natural convection of liquid PCM [21]. Pouyan et al. investigated the vertical phase change thermal storage system with added copper metal foam by numerical simulation in terms of porous media modeling, multi-segmented metal foam, etc., and showed that the addition of copper foam was able to reduce the melting time by 85% [22]. Mohammad and Duan conducted a numerical study on heat-storage equipment with a shell and tube structure. The results demonstrated the addition of nanoparticles (Al_2O_3) to PCM does not accelerate the melting process, but raises the flow resistance of the melted PCM significantly, thus prolonging the charging time [23]. Thirdly, the heat flux can be enhanced by micro-encapsulation [24] or macro-encapsulation [25] of PCM. There is also a study of using multiple PCM materials in series to link up multi-chambers, i.e., cascaded PCMs, to achieve flatter power input/output. Gerard et al. conducted comparative experiments using d-mannitol and o-benzoquinone. Experimental results showed a 19.36% increase in the efficiency of the multi-PCM structure and higher uniformity in the inlet/outlet temperature difference compared to the single PCM structure [26].

In addition, lots of researchers carried out studies in other aspects. Fadl et al. proposed a vessel featuring a rectangular section and used paraffin RT44HC as the PCM. This vertically arranged, multi-channel, tubular LHS system, demonstrated a reduced charging time of 3.5 h when the HTF inlet temperature increased from 60 to 70 °C, and an additional 2 h reduction in melting duration upon further increasing the HTF inlet temperature to 80 °C. [27]. Khobragade and Devanuri conducted a study on the simultaneous charging and discharging processes through a shell-tube heat exchanger, employing lauric acid as the PCM. The research revealed that increasing HTF's temperature has a substantial impact on improving the charging process while decreasing the temperature of the cold fluid has a greater effect on the vertical structure. [28]. They also used a transient numerical simulation of its temperature distribution and liquid fraction. They found that the liquid fraction increased by 38.02% with the stored energy increased by 26.2% as the inclination angle went from 90° to 0° [29].

Muhammad et al. researched the impact of using asymmetric fins on the TES. The researchers concluded that the application of asymmetric fins led to a 74.3% decrease in the charging time and a 43.7% improvement in the stability of the rate. In comparison, the asymmetric fins enhanced the convection and increased the Nusselt number of the discharging process by 80.2% [30]. Appolinaire et al. performed an improvement study on this basis, and the paper indicated that the improved proposal reduced the time of heat storage and exothermic processes by 10%−47%, respectively [31]. Kumar et al. carried out experimental and numerical studies on the melting behavior of lauric acid in a shell and tube tank featuring horizontal fins and inner tubes positioned at various eccentricities. The results indicated that the maximum eccentric position led to a 21% enhancement in the melting rate compared to the concentric position [32]. Guedri et al. comparatively evaluated the performance of their system using a different number of leaves (single, double, triple, and quadruple fins) with the same torsion angle. The findings substantiated the conclusion that the performance is superior for the double-fin system and triple-fin system, with their solidification times reduced by 30.43% and 15.78%, respectively, relative to the single-fin configuration [33]. Mohammadreza et al. proposed the use of a truncated pipe instead of the straight pipe and optimized the simulation of the gap between the truncated pipe and the outer pipe. Their experimental results showed that the case of a gap width of 5 mm had the best results, and compared to the case of a straight pipe was able to save 25.6% of the melting time, and improve the heat storage rate of 32.8% [34]. Most research on LHS systems focused on improving fin shapes, and most of them were devoted to low-temperature LHS in terms of their applied temperatures. The existing studies on the performance of LHS mostly focus on analyzing the rule of PCM temperature [35], system efficiency [36], and mechanism [37].

To sum up, the research on high temperature phase change materials should be paid attention. In order to solve the above problems, this paper chooses spiral fins (due to its widely applications) and innovatively builds a single-tube visible LHS system, aiming at revealing the influence of HTF flow rate and inlet position on the thermal performance of TES system by taking spiral fins as an example. The experimental results provide some valuable data and references for LHS's utilization of renewable energy.

2. Equipment and procedures

2.1. Experimental equipment

The experiment employed a small-scale, vertical, single-tube visualization bench, which mainly consisted of the following components: heat transfer fluid system, storage system, cooling system, and acquisition system. The experimental apparatus is illustrated in Fig. 1.

Fig. 2 presents the experimental apparatus, showing the layout of each experimental device. Fig. 2(a) is the front and side view of TES, which consists of the outer rectangular shell covering insulation, with external dimensions of 250 mm × 250 mm × 2000 mm and the thickness of 2 mm; the insulation binds up the subject of the shell-tube exchanger, which is cylindrical with the size of 121 mm × 4 mm. The viewing window is installed on a plane 47.5 mm from the center of the cylinder, with slots cut from the top and bottom of the pipe 50 mm from each end. The quartz window is secured using a pressed plate structure to ensure tightness and prevent PCM leakage during melting.

Fig. 3 points out the specific dimensions. The central component is the tube and fins, featuring outer and inner diameters of 32 mm and 26

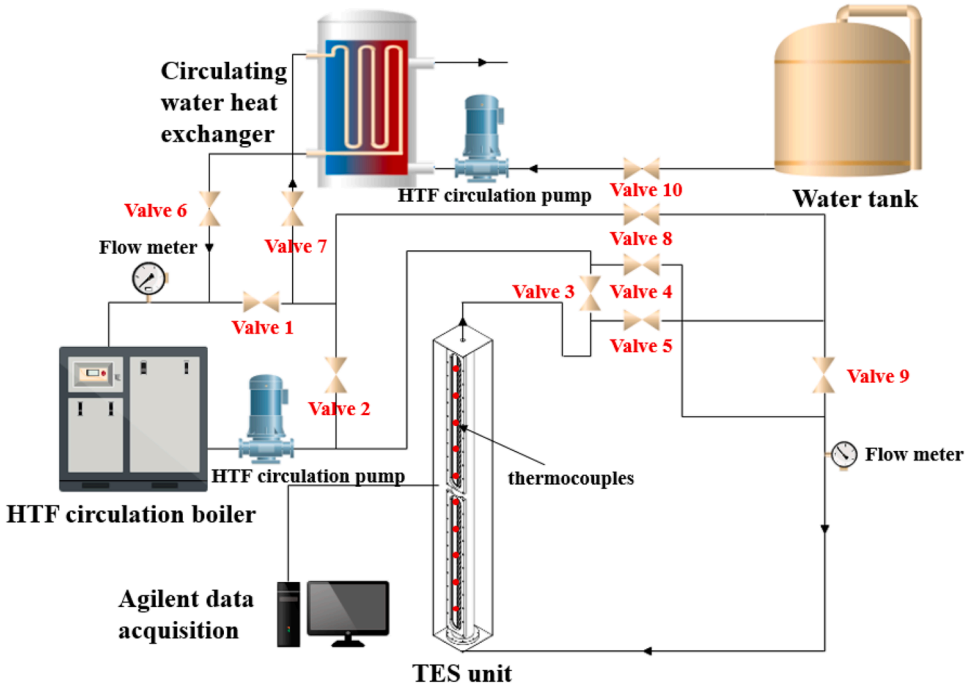

Fig. 1. System flow schematic of LHTES in discharging.

Fig. 2. (a)Front/side view of TES (b) heat transfer fluid system.

mm, respectively, and a height of 1980 mm. The fins are uniformly distributed along the tube, with a width of 15 mm and a spacing of 1.5 mm. Fig. 4 shows the precise dimensions and structural configuration. It should be noted that PCM is distributed between the shell and the finned tube, and the part between each pinch of the spiral fin is also filled with PCM. After modeling the finned tube by Solidworks, the surface of the spiral fin and the contact part between the heat exchange tube and PCM are counted by the measuring tool provided by the software. The measuring tool shows that the heat exchange area is 9100.4 cm^2, the total volume of finned tubes is 23.38 dm^3 (tube volume is 22.47 dm^3 and fin volume is 0.91 dm^3).

Fig. 2(b) shows the heat transfer fluid system, which mainly consists of four parts: boiler for heating thermal conductive oil, HTF pipeline, oil tank, and pump. A thermal oil boiler was used to heat the low-temperature HTF by electricity, which is driven by a pump to the TES.

The acquisition system is designed to monitor the temperature variations of the HTF both before and after passing through the TES system, as well as PCM's temperature. Furthermore, the flow rate of HTF needs to be tracked by a flow meter. Fig. 3 depicts the arrangement of thermocouples, with thermocouples #1–10 employed to observe the temperature distribution of PCM, while thermocouples #11 and #12 are used to monitor the temperatures of HTF. As can be seen from the A-A

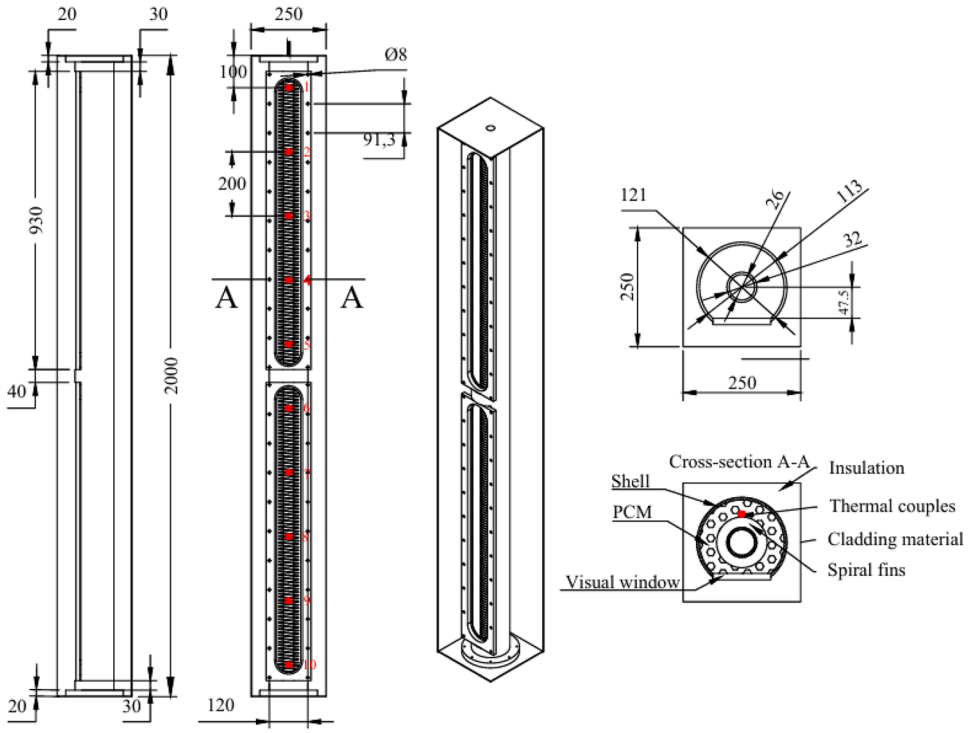

Fig. 3. Model diagram of TES.

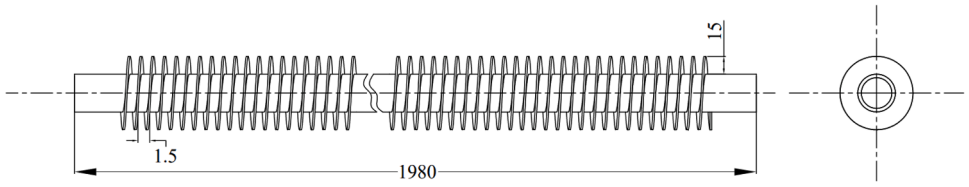

Fig. 4. Model diagram of the spiral finned tube of TES.

cross-sectional view, the thermocouple is arranged in the PCM next to the edge of the fin. It's owing to the thermocouples can only be placed from the top after the installation of the experimental platform and before adding solar salt.

2.2. Properties of the materials

The stable properties of PCM ensure the safety of the experiment, which is a significant advantage of PCM, leading to its widespread adoption. Solar salt is utilized as the PCM in this experiment. It has been tested in practice for a long time and mainly contains $NaNO_3$ and KNO_3. In the charging stage, the solar salt is converted from solid to liquid and reverted to solid as the discharging stage progresses.

The TG/DSC testing can reveal the thermal physical properties of PCM within a temperature range. The phase change heat is obtained by averaging the experimental temperature range (190–270 °C) according to the TG-DSC test data. In the TG/DSC test, nitrogen atmosphere was used, and the temperature was heated from room temperature to 300 °C at 10 °C/min, and the output was once every 3 s. The properties of the material used in this experiment are as follows: in the process of charging, the initial melting temperature, complete melting temperature, and fastest melting temperature are 210.75 °C, 262.58 °C and 226.73 °C, respectively, and the enthalpy of the PCM in this process is 128.15 kJ/kg; correspondingly, the discharging process involves parameters of 252.14 °C, 199.03 °C, 259.29 °C, and 125.00 kJ/kg, respectively.

Therminol l-60 heat conductive oil is the HTF in this study, the product is produced by Hemai New Energy Technology (Shanghai) Co., Ltd., and it has been tested by more than 9000 cycles, and it has good safety and stability, and passed the third-party tests such as toxicity and corrosiveness. It enables the heat transfer fluid system to operate reliably, stably, and continuously in a range of −20 to 330 °C. In this experiment, the operating temperature range of HTF is 170–290 °C, with corresponding specific heat capacity, thermal conductivity, and viscosity of 1.950–2.520 kJ/(kg·K), 0.1112–0.096 W/(m·K), and 0.925–0.408 mPa·s, respectively. The detailed thermal characteristics are presented in Table 2.

2.3. Procedure of the experiment

During the experimental process, it is crucial to determine the flow direction of HTF in TES. By opening valves (3 and 9) and closing valves 4 and 5, HTF can flow from the upper portion of TES into the system. On the contrary, it enters from the bottom into the system. Once the valves are adjusted to satisfy the HTF flow direction of the experiment, the preheating stage initiates. During preheating, HTF is warmed from its initial temperature to a predetermined set point of 190 °C. Generally, the temperature will be set higher than 190 °C due to the loss by pipeline. According to the pre-experiment, setting the boiler's temperature to 200 °C is more appropriate. The process of preheating is complete when the T_{ave} of PCM in TES (#1–10 thermocouples' average temperature) reaches 188±1 °C.

Table 1
Properties of the PCM, HTF, and carbon steel [38].

Properties	Symbol	Units	PCM (190/270 °C)	Oil (170/290 °C)	Carbon steel
Density	ρ	kg/m^3	2213.5/1924.6	892/792	7850
Peaking melting/solidification temperature	T	°C	225.35/219.90	–	–
Latent heat	ΔH	kJ/kg	117.0/120.0	–	–
Specific heat	c_p	kJ/(kg·K)	1.536	1.950/2.520	0.47
Thermal conductivity	k	W/(m·K)	0.503	0.1112/0.096	48.85
Dynamic viscosity	μ	mPa·s	4.34	0.925/0.408	–

Table 2
Table of HTF properties varying with temperature.

Temperature °C	Density kg/m^3	Cp kJ/(kg·K)	H kJ/kg	Λ W/(m·K)	Viscosity cSt
170	892	1.95	506	0.1112	0.925
180	884	1.99	502	0.1102	0.844
190	876	2.04	497	0.1091	0.774
200	868	2.09	492	0.1079	0.714
210	860	2.13	487	0.1067	0.661
220	852	2.18	482	0.1055	0.615
230	844	2.23	476	0.1043	0.574
240	835	2.27	471	0.103	0.538
250	827	2.32	465	0.1016	0.506
260	818	2.37	459	0.1003	0.478
270	810	2.42	452	0.0989	0.452
280	801	2.47	446	0.0974	0.429
290	792	2.52	439	0.096	0.408

As the experimental process typically involves constant-temperature heat storage, after preheating is complete, the temperature of HTF needs to rise to the experimental operating condition (290 °C). The HTF should be heated to 290 °C in a separate circulation loop to guarantee the accuracy and reliability of the experiments. It refers to the external circulation. At this point, valve 2 in Fig. 1 is open, and valve 3 is closed, allowing HTF to flow in a closed loop and no longer through the TES system. The temperature of HTF will increase to the set temperature in about 5 min after adjusting the controller of the HTF boiler. Then, open valve 3, close valve 2, and the data acquisition system is activated, marking the official start of charging (as seen in Table 3). The internal temperature of TES will gradually increase, and the charging stage is complete when the average temperature reaches 270 °C. After that, it is necessary to open valve 2 and close valve 3. Adjust the temperature setting of the boiler and activate the cooling system pump to allow the HTF temperature to decrease. HTF is reheated by the HTF boiler, flowing through the valves 4 and 5 to the TES, which refers to the discharging process (as seen in Table 4).

In addition, after recording and fitting the flow data, the monitoring of flow rates can be simplified to record data every 5 min. Additionally, this experiment features visualization, which involves removing the insulation layer surrounding the viewing window to capture images of the PCM.

Taking the charging process as an example, as shown in Fig. 5, the finned tube is vertically placed, high temperature HTF enters from the upper part and flows out from the lower junction, and PCM is filled near the finned tube. On the one hand, HTF at high temperature conducts heat with nearby PCM through the inner wall of the pipeline, and on the other hand, it also exchanges heat through fins. After the phase change material near the fin tube becomes liquid (Fig. 6), the heat is first exchanged to the liquid PCM, and then to the solid PCM farther away from the fin, and at the same time, natural convection will occur under the action of gravity due to the change of density.

Table 3
Valves condition during charging.

Opened valves	Valve 1, Valve 3, Valve 8, Valve 9
Closed valves	Valve 2, Valve 4, Valve 5, Valve 6, Valve 7, Valve 10

Table 4
Valves condition during discharging.

Opened valves	Valve 4, Valve 5, Valve 6, Valve 7, Valve 8, Valve 10
Closed valves	Valve 1, Valve 2, Valve 3, Valve 9

2.4. Experimental condition

This study employed three different flow rates of 33, 26.4, and 19.8 L/min to examine the influence of HTF flow rate on the efficiency of TES, corresponding to Cases I-III. Modifying the inlet position of HTF is feasible, and previous experiments have shown that HTF has always entered TES from the bottom. Therefore, to investigate whether the direction of HTF affects the system's thermal efficiency during charging and discharging, we conducted experiments by Case I, altering the direction of HTF and comparing the results, as seen in Cases IV-VI. The specific start and end times for each condition are in Table 5.

In addition, the thermal power exhibits significant fluctuations over time in this experiment. However, in practical applications, more stable power output/input can significantly enhance the applicability of PCM in peak shaving. Therefore, this experiment also established a graded heating condition. It involves maintaining a steady T_{gap} within a narrow range. As shown in Table 6, the temperature difference was maintained at approximately 45–50 °C.

3. Calculation methodology

The thermal performance metrics of primary concern in this study include the charging efficiency and discharging efficiency, as well as the cycle efficiency. The following need to be obtained to calculate these parameters: specific flow rate of HTF, temperatures of HTF before and after flowing through TES, internal temperature of PCM, and time of charging and discharging.

After obtaining the flow rate in volume and temperatures of HTF, the instantaneous power of HTF can be calculated using Eq. (1):

$$P_{inst} = \rho v c_{p,HTF} |T_{in} - T_{out}| \quad (1)$$

Where "ρ" represents HTF's density and "v" denotes its flow rate in volume. "ρ" is determined by linear interpolation of the temperature; "$c_{p,HTF}$" is the specific heat of the HTF, the specific value is shown in Table 1; "T_{in}" and "T_{out}" refer to HTF's temperature before and after the entry of TES, respectively.

The cumulative energy of HTF is calculated by Eq. (2):

$$E_{HTF} = \int_0^t P_{inst} dt \quad (2)$$

Where E_{HTF} denotes the cumulative energy of HTF, t represents the time elapsed during the charging or discharging.

"E_{PCM}" denotes the energy absorbed by PCM in the charging or the energy released by PCM in the discharging process, calculated by Eq. (3):

$$E_{PCM} = c_{PCM} \bullet m_{PCM} + c_{p,PCM} |T_1 - T_0| \bullet m_{PCM} \quad (3)$$

Where "c_{PCM}", "m_{PCM}", and "$c_{p,PCM}$" are melting heat (the value in this study is 122 kJ/kg), mass, and HTF's specific heat, respectively; T_1 and T_0 are the average temperatures of thermocouples at the end of

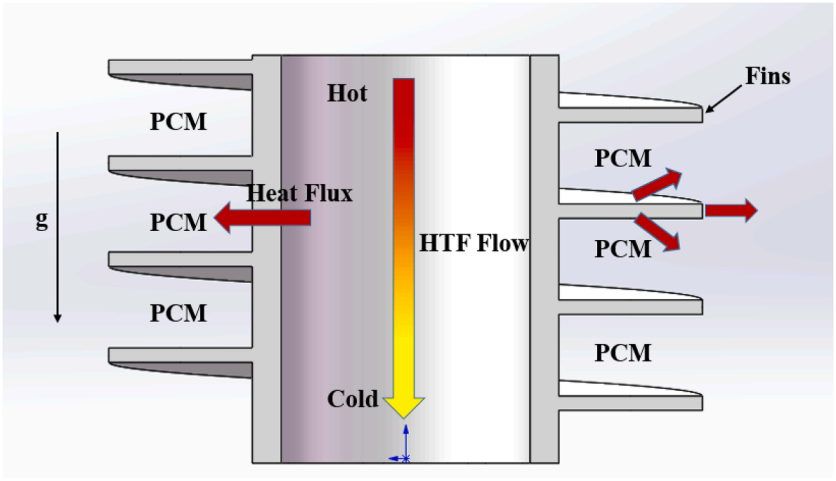

Fig. 5. Schematic diagram of heat transfer in charging process.

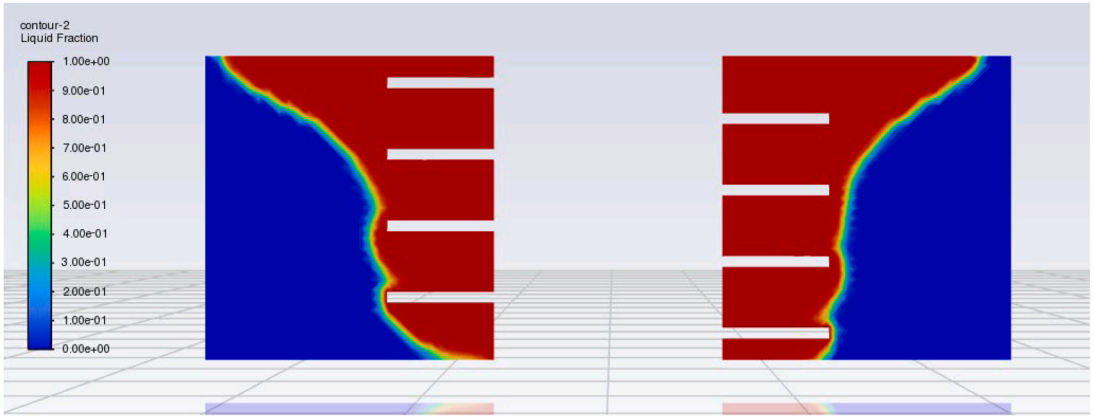

Fig. 6. A diagram in the simulation of helical fins at one moment.

Table 5
Experimental conditions table.

	Case I	Case II	Case III	Case IV	Case V	Case VI	Case VII
Endothermic Temperature (°C)	270	270	270	270	270	270	–
Endothermic Oil Inlet Direction	down	down	Down	down	up	up	down
Exothermic Temperature (°C)	190	190	190	190	190	190	–
Exothermic Oil Inlet Direction	up	up	Up	down	down	up	–
HTF flow rate (L/min)	33	26.4	19.8	33	33	33	33

charging and the beginning of charging, respectively.

The charging efficiency and discharging efficiency are calculated as shown in Eqs. (4)(5):

$$\eta_s = \frac{E_{PCM}}{E_{HTF}} \tag{4}$$

$$\eta_d = \frac{E_{HTF}'}{E_{PCM}'} \tag{5}$$

Where "η_s" and "η_d" represent the charging efficiency and discharging efficiency, respectively.

Table 6
Temperature rise data sheet for Case VII.

Stage	Temperature of the TES unit(°C)	Oil flow rate(L/min)	Temperature of thermocouple #1(°C)	Inlet temperature of the oil (°C)
1	190–200	33	178.1	250
2	200–210	33	189.0	255
3	210–220	33	200.0	260
4	220–230	33	209.3	265
5	230–240	33	218.6	280
6	240–250	33	223.8	285
7	250–260	33	230.1	290

The cycle efficiency after one cycle is calculated by the following equation:

$$\eta_{total} = \frac{E_{HTF}'}{E_{HTF}} \tag{6}$$

Furthermore, since experimental instruments inherently possess errors, a thorough uncertainty analysis is also imperative to guarantee the precision and reliability of the experimental outcomes. In this experiment, the primary sources of uncertainty are the thermocouples and flow meters. Below, we will calculate the uncertainty using the Kline-McClintock method [39,38]. If there are i independent variables x_i that affect the parameter W, then the uncertainty of W, ΔW, can be calculated by combining the uncertainties of each variable:

$$\Delta W = \sqrt{\sum_{1}^{i}\left(\frac{\partial W}{\partial x_i}\Delta x_i\right)^2} \tag{7}$$

The specific uncertainties in the text are presented in Table 7.

4. Results and discussion

In the following seven operating conditions of this experiment, we will first analyze three operating conditions with various flow rates to elucidate the specific effect on the thermal efficiency of system via energy relationships subsequently, we will derive the connection between the directions of charging and HTF inlet/outlet by comparing the efficiency and visualizing the temporal trend of PCM melting in the visualization images; finally, we will verify whether adjusting the T_{gap} between HTF and PCM can stabilize the efficiency of heat storage and release through instantaneous efficiency plots of the graded heating operating conditions.

4.1. Impact of different HTF flows on TES

To examine the influence of flow rate on the efficiency of TES, three experiments were conducted under this condition, with the beginning and end of charging temperatures maintained consistent throughout. Under charging temperatures of 190–270 °C, Case I-III were conducted at flow rates of 33, 26.4, and 19.8 L/min, respectively. During the experiment, the flow rate was recorded, and the data of the thermocouple was collected using the acquisition system. After the experiment, the data was processed to obtain the following information: the charging and discharging times, corresponding HTF inlet and outlet temperatures and temperature differences, trends of temperature changes with charging time for different heights of PCM, average temperature of the thermocouples, instantaneous power and cumulative output/input energy of the HTF, as well as charging/discharging efficiency and cycle efficiency, etc.

4.1.1. Charging and discharging time

The times spent during charging or discharging of the three experiments can be obtained from Fig. 7, with charging times of 3805, 5135, and 5695 s, and discharging times of 2720, 3225, and 4260 s. According to the experimental results, we take Case III as the benchmark working condition. The charging rate in the figure compares the ratio of energy to time at other flow rates with that of 19.8 L/min. The experimental outcomes reveal that as the flow rate is elevated, the charging duration and discharging duration exhibit a similar downward trend. A closer examination reveals that the 9.83% reduction in charging time resulting from an increase from 19.8 L/min to 26.4 L/min is significantly less than the 25.9% reduction in charging time with flow rate increases from 26.4 to 33 L/min; conversely, the time reduction from 26.4 to 33 L/min in discharging process is lower than that from 19.8 to 26.4 L/min. Specifically, the enhancement is more significant at higher flow rates during the charging process. However, the enhancement is more pronounced when at a lower flow rate for the discharging process.

4.1.2. Temperatures at the inlet and outlet of HTF

Fig. 8 depicts the temperature changes of HTF over time, showing similar trends for the three experiments. During the charging, the temperature curve changes rapidly (90–95%) in the first ten minutes. And it becomes smoother as the accumulated heat increases until the charging process is complete. A closer inspection of the local magnification of Fig. 8 reveals that the curve of T_{inlet} displays more variability, whereas the T_{outlet} curve is significantly smoother. That is due to the delayed response of the temperature control program of the boiler. While the charging process is theoretically considered a constant-temperature process, in practical implementation, only the temperature of the outlet and HTF tank can be monitored. When the HTF temperature falls below a specific threshold, the heating program control starts the heating element to initiate heating. Similarly, when the oil temperature exceeds the set value, the heating element will stop, ultimately causing the HTF outlet temperature to oscillate around the set temperature within a small range. Owing to the lower T_{gap}, the oscillating temperature of HTF has a negligible impact on the charging, ultimately yielding a stable T_{outlet} from TES.

Furthermore, at the initial time point, due to the same preheating temperature and set temperature of charging, the initial temperatures of the HTF should be the same. However, since the valve needs to open manually, and the flow rates of HTF are different, the hot HTF flows through the TES before the valve is fully adjusted, which results in a higher initial temperature for the experiment with the higher flow rate.

As seen in Fig. 9, the T_{inlet} and T_{outlet} of HTF during the discharging also exhibit similar trends. Upon closer examination of the local enlargement of the figure, it is clear that the outlet temperatures of the experiment with higher flow rates decrease more rapidly. But at around 20 min, the temperatures of the three experiments converge.

Table 7
Properties and uncertainties of TES under different operating conditions.

	Case I'	Case II'	Case III'	Case IV	Case V	Case VI
P_{ave} (charging) (kW)	2.34±0.09 (4.05%)	2.22±0.08 (3.52%)	1.88±0.065 (3.45%)	2.69±0.08 (3.02%)	2.61±0.08 (3.16%)	2.27±0.09 (4.19%)
P_{ave} (discharging) (kW)	1.829±0.08 (4.48%)	1.706±0.07 (3.99%)	1.572±0.06 (3.68%)	1.86±0.08 (4.42%)	1.856±0.07 (3.88%)	1.791±0.08 (4.62%)
E_{cum} (injected) (kJ)	8709.9 ± 235 (2.70%)	10,624.1 ± 223 (2.10%)	12,078.4 ± 159 (1.32%)	12,164.1 ± 211 (1.73%)	10,893.3 ± 194 (1.78%)	8991.1 ± 210 (2.33%)
E_{cum} (released) (kJ)	5082.8 ± 176 (3.46%)	5563.3 ± 135 (2.73%)	5439.3 ± 118 (2.18%)	5360.6 ± 168 (3.13%)	5346.6 ± 164 (3.07%)	4871.3 ± 168 (3.45%)
Cycle Time(s)	7425	8155	9875	7390	8335	7655
Cycle efficiency	58.35%	52.36%	45.05%	47.69%	44.97%	54.18%

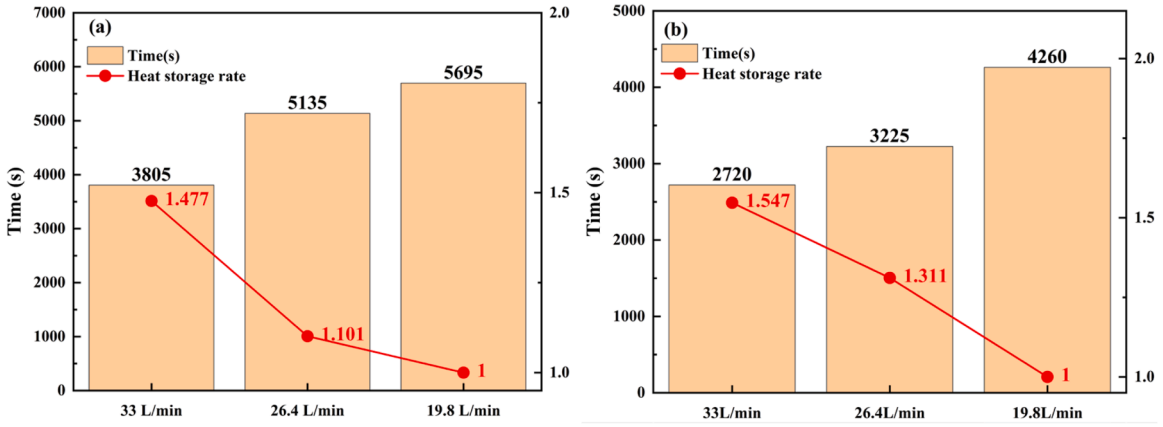

Fig. 7. (a)Charging times at different flow rates. (b)Discharging times at different flow rates.

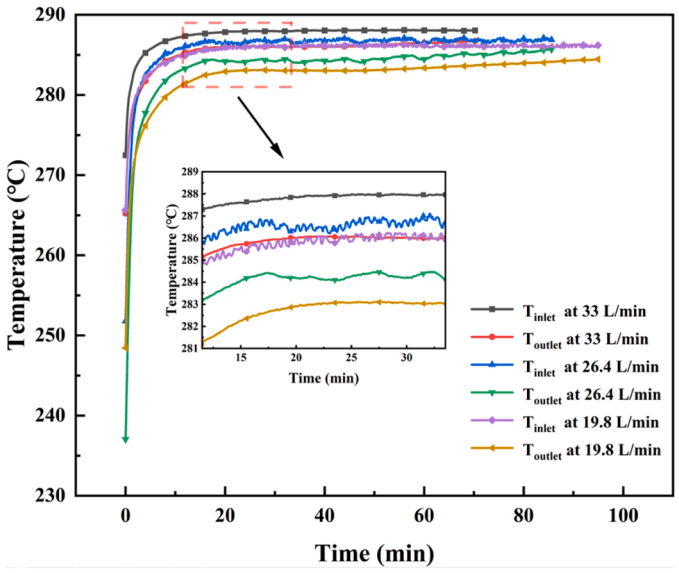

Fig. 8. Plot of inlet and outlet temperature of heat transfer oil during charging.

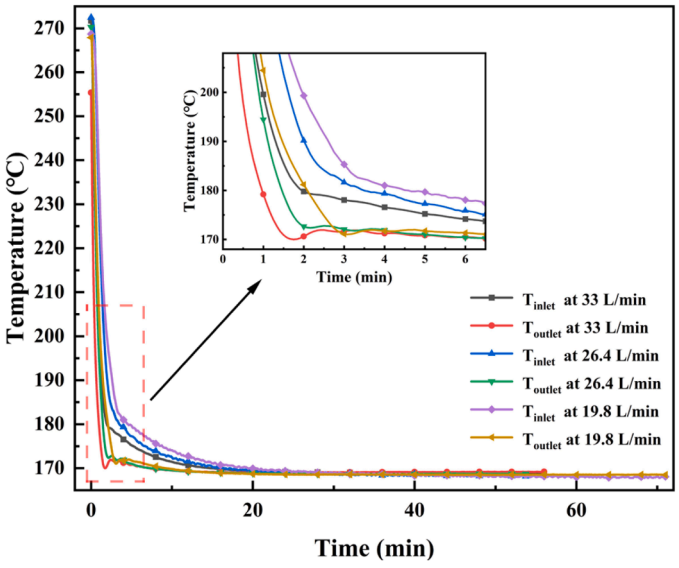

Fig. 9. Plot of inlet and outlet temperature of heat transfer oil during discharging.

4.1.3. *Temperature variation of PCM at different heights*

Due to the similar trends in PCM temperature curves under different flow rates (see average temperature curve in Fig. 11), and the more pronounced changes in temperature curves at higher flow rates, the following discussion will focus only on the temperature change rules of PCM under 33 L/min HTF flow rate.

Fig. 10(a) shows PCM's temperature variations at varying heights during charging. Due to the proximity of #1 and #10 thermocouples to the boundary of the TES, heat loss is severe, and their temperature deviations are higher than those of the other thermocouples. Consequently, the data from these two thermocouples was excluded. The temperature curves of #2–9 all exhibit a clear inflection point, which occurs approximately 15 min after the start of charging. The temperature difference curve in Fig. 11(a) shows that the temperature difference of HTF also becomes stable around 15 min, corresponding to a temperature of approximately 260 °C, which is consistent with the properties of solar salt mentioned earlier. Thermocouple #5 deviates from the other data, with neighboring #4 and #6 thermocouples displaying similar temperatures and trends. The iron wire used to secure thermocouples to the heat exchanger tube may lead to slight loosening. Initially, it was suspected that the #5 thermocouple did not fix properly, resulting in a wider distance between the thermocouple and the tube, causing the surrounding PCM to warm up primarily through heat conduction after the central PCM is heated. As the time increases to 45 min, #5 thermocouple gradually approaches the temperature of #4 and #6 thermocouples, indicating that #5 thermocouple did not suffer from damage, and this also confirms the reasonability of our hypothesis.

As shown in Fig. 10(b), the temperatures of all thermocouples at different heights exhibit a downward trend, and the slopes of the curves gradually decrease. Additionally, the initial distribution of PCM's temperature at different heights is generally consistent with that at the end of charging. Notably, the PCM temperatures at the edges of the TES are found to be lower than those in the central region. That is due to the sealing properties of the insulation materials at the edges.

For the temperature curve of the #9 thermocouple, the initial temperature is the lowest due to the HTF flowing from the bottom into the TES, and it also has the highest temperature gradient in a certain period. However, as the temperature of PCM decreases, it can be known from the thermal properties in Table 2 that solar salt begins to solidify at around 252 °C. The heat transfer from the lower PCM causes the temperature of the HTF to rise, thereby reducing the temperature gradient in the upper region and leading to a gradual decrease in temperature. Following the transfer of heat from the lower PCM, which is approximately complete after 20 min (as depicted in Fig. 9), the gradient of temperature between the upper PCM and HTF increases, facilitating accelerated heat transfer from the upper layer.

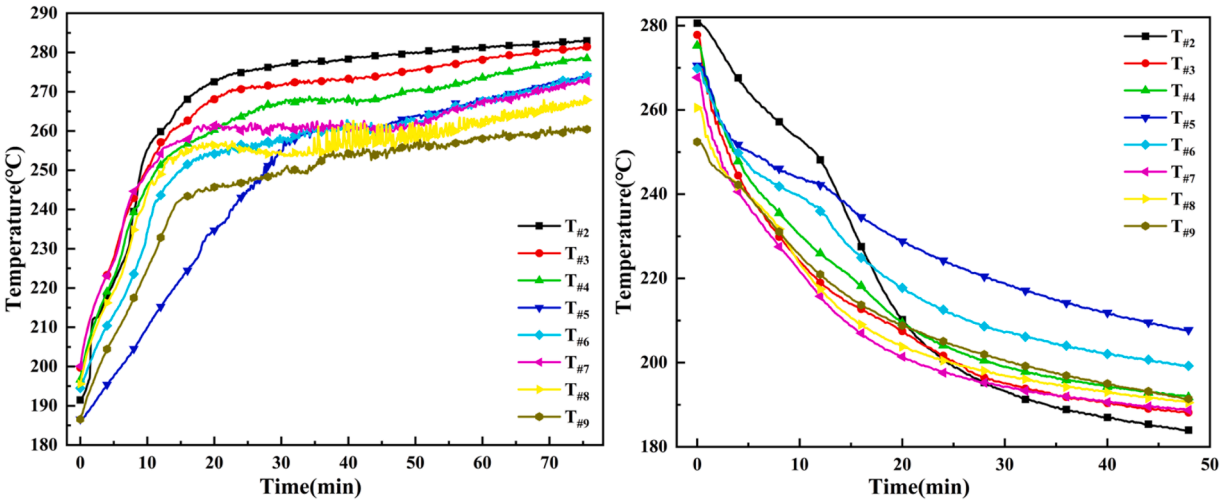

Fig. 10. Temperature Plot of #2–9 thermocouples during(a) charging (b) discharging in Case I.

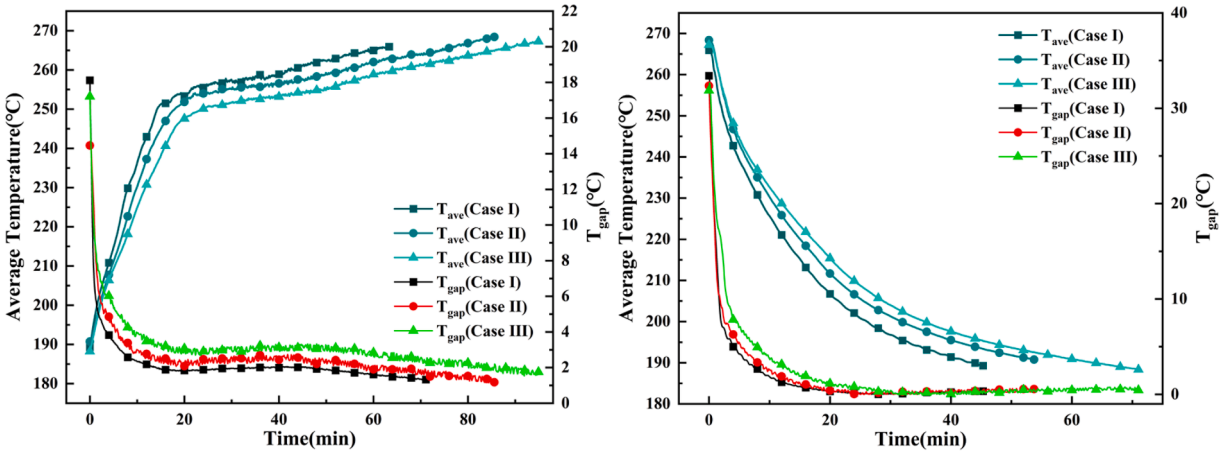

Fig. 11. Average temperature of #1–10 thermocouples and temperature gap between inlet and outlet of heat transfer oil during(a)charging (b)discharging.

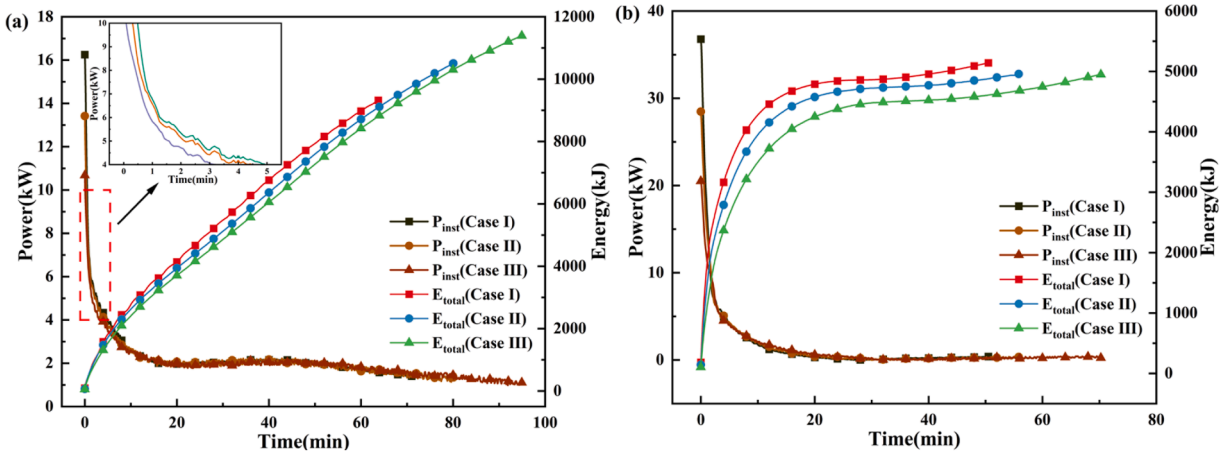

Fig. 12. Instantaneous power and cumulative energy of heat transfer oil in(a)charging (b)discharging.

4.1.4. Charging and discharging efficiency of TES

Fig. 12 depicts the instantaneous power and cumulative energy curves under various flow rates. The overall trend of the instantaneous power curve is in line with the temperature difference curve in Fig. 11. However, the temperature difference is higher for the low-flow-rate experiment, yet the corresponding instantaneous power is lower. It suggests that temperature difference and instantaneous power is a non-linear relationship, as evident from Eq. (1). It indicates that they are influenced by both mass flow rate and specific heat capacity. This non-linear relationship highlights the complexity of the thermodynamic

performance of the system.

Additionally, significant differences in cumulative energy under various flow rates during charging were observed (9335.7, 10,053.3, and 11,390.4 kJ). In contrast, the impact of flow rate on total heat released during discharging is relatively low (5142, 4958, and 4949 kJ), with instantaneous power changes being relatively lower. In practical applications, a large-flow-rate charging and small-flow-rate discharging method can be employed to achieve a more stable power output. Uncertainty calculations revealed that the uncertainties in cumulative energy under different flow rates during storage are 230.00, 192.35, and 157.44 kJ, corresponding to relative uncertainties of 2.46%, 1.91%, and 1.38%(as seen in Table 7). These data indicate that elevating the flow rate of HTF can diminish energy loss.

Besides the cumulative energy of HTF, the efficiency between PCM and HTF is also a crucial parameter. As shown in Fig. 13(a), for the three experiments with flow rates of 33, 26.4, and 19.8 L/min, the energy stored in PCM is approximately the same, at 7531.5, 7486.4, and 7538.0 kJ, respectively. By combining the cumulative energy of HTF, the charging efficiency of each experiment was calculated using Eq. (4), yielding values of 80.67%, 74.47%, and 66.18%, respectively. The remaining energy is either lost through the pipeline and TES system to the environment or used to overcome energy losses during transmission. The released energy during discharging is a part of the stored heat energy in PCM, and the switching time from charging to discharging takes 3–5 min. It leads to a loss of approximately 10 kJ. The release process of the three experiments released 5262.1, 4958.2, and 4949.2 kJ of heat energy to HTF, respectively, and the discharging efficiency was calculated using Eq. (5), which are 69.98%, 66.34%, and 65.71%, respectively. Fig. 13(b) shows the ratio of $E_{HTF'}$ during discharging to E_{HTF} during charging, which is the cycle efficiency. The results indicate that as the HTF flow rate rises from 19.8 L/min to 33 L/min, the cycle efficiency rises from 43.45% to 56.36%. The data above indicates that raising the flow rate of HTF is beneficial for improving the efficiencies, with the influence of increased flow rate being more significant on charging than on discharging.

At higher HTF flow rate, according to the *Re* formula in the pipeline, at the same temperature, *Re* is directly proportional to the flow rate, and *Re* will be larger at higher flow rate. In the process of charging, the temperature difference between the inlet and outlet of the heat transfer oil is relatively small due to the high flow rate, that is, the temperature inside the fin tube is higher, so the temperature gradient is larger. While the density and viscosity are smaller and Pr is larger when the HTF temperature is higher, which has better heat diffusion performance. In addition, PCM has better thermal conductivity after melting, and most of the melted PCM gathers in the upper part of TES system due to density, which is more conducive to the transfer of heat to solid PCM. During discharging process, PCM in TES system is in liquid state, solidification occurs near the finned tube first. Due to the poor thermal conductivity of solid PCM, HTF flow rate has no obvious effect on heat transfer enhancement.

Additionally, to mitigate the effect of HTF flow direction on the test results, supplementary tests were conducted where HTF flows in opposite flow directions at the same flow rate (designated as Case I', II', and III'). The results demonstrate that the cycle efficiency increases with increasing flow rate, achieving values of 45.05%, 52.36%, and 58.12%, respectively. In light of these results, it is evident that the cycle efficiency exhibits a similar relationship with flow rate as seen in Cases I-III, and further analysis reveals that the cycle efficiency consistently peaks when HTF enters the TES from the top. Therefore, this paper will delve into the effect of HTF inlet position on the property of TES in the next section.

4.2. Impact of HTF import location on TES

To comprehensively investigate the impact of operating parameters on the system, this paper also conducted a study on HTF inlet, maintaining the flow rate of 33 L/min and performing three experiments (Cases IV-VI). A comparison framework is established with Case I, and Table 5 provides a detailed list of experimental parameters. A comparison of each experiment will be conducted to investigate the influences of inlet position on the charging, discharging, and cycle efficiency.

4.2.1. Effect of different inlets on charging

The charging time is significantly affected by different inlet directions, as illustrated in Fig. 14(a). The average charging time from the bottom into the TES is 82.5 min, whereas from the top into the TES, it is 76.25 min, with a relative reduction of 7.57%. The figure also clearly shows that the experimental charging efficiency of HTF entering from the top into TES is approximately 10% higher than that of HTF entering from the bottom.

Fig. 14(b) presents the temperature profiles of HTF, which exhibit a consistent trend: the HTF temperature rapidly reaches 285 °C within the first 10 min of charging and remains relatively constant. The experimental process shows that HTF is preheated to a temperature of 200 °C, whereas the figure indicates that HTF temperature begins to rise from 250 °C. The HTF in the pipeline has not returned to the boiler when the

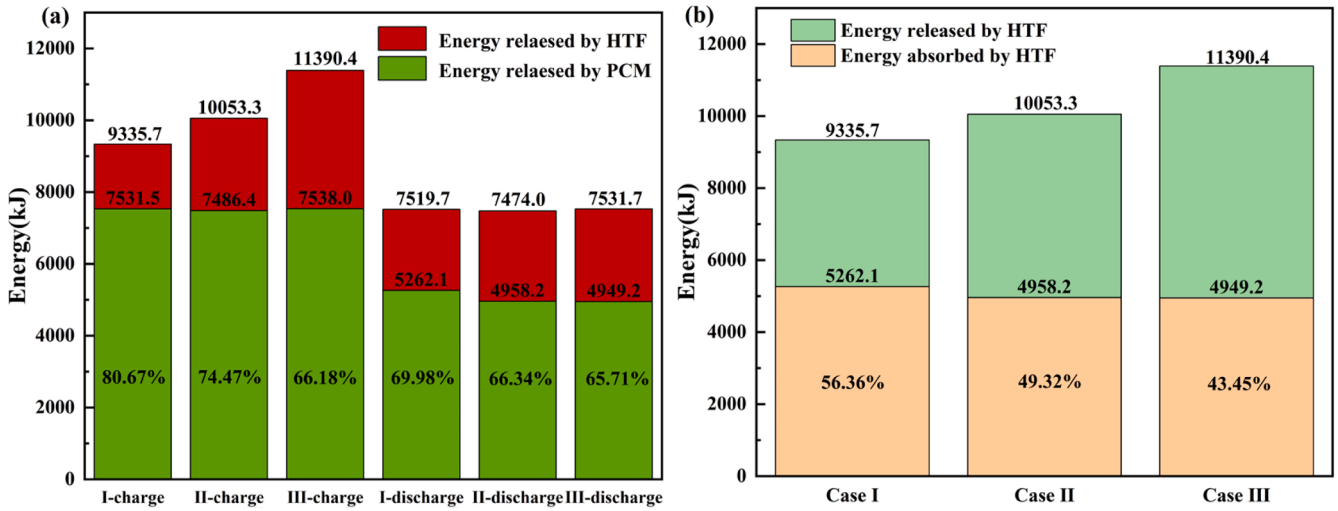

Fig. 13. Plot of efficiency at different flow rates in(a)charging (b)discharging. (The energy in the upper part of the diagram contains the lower energy).

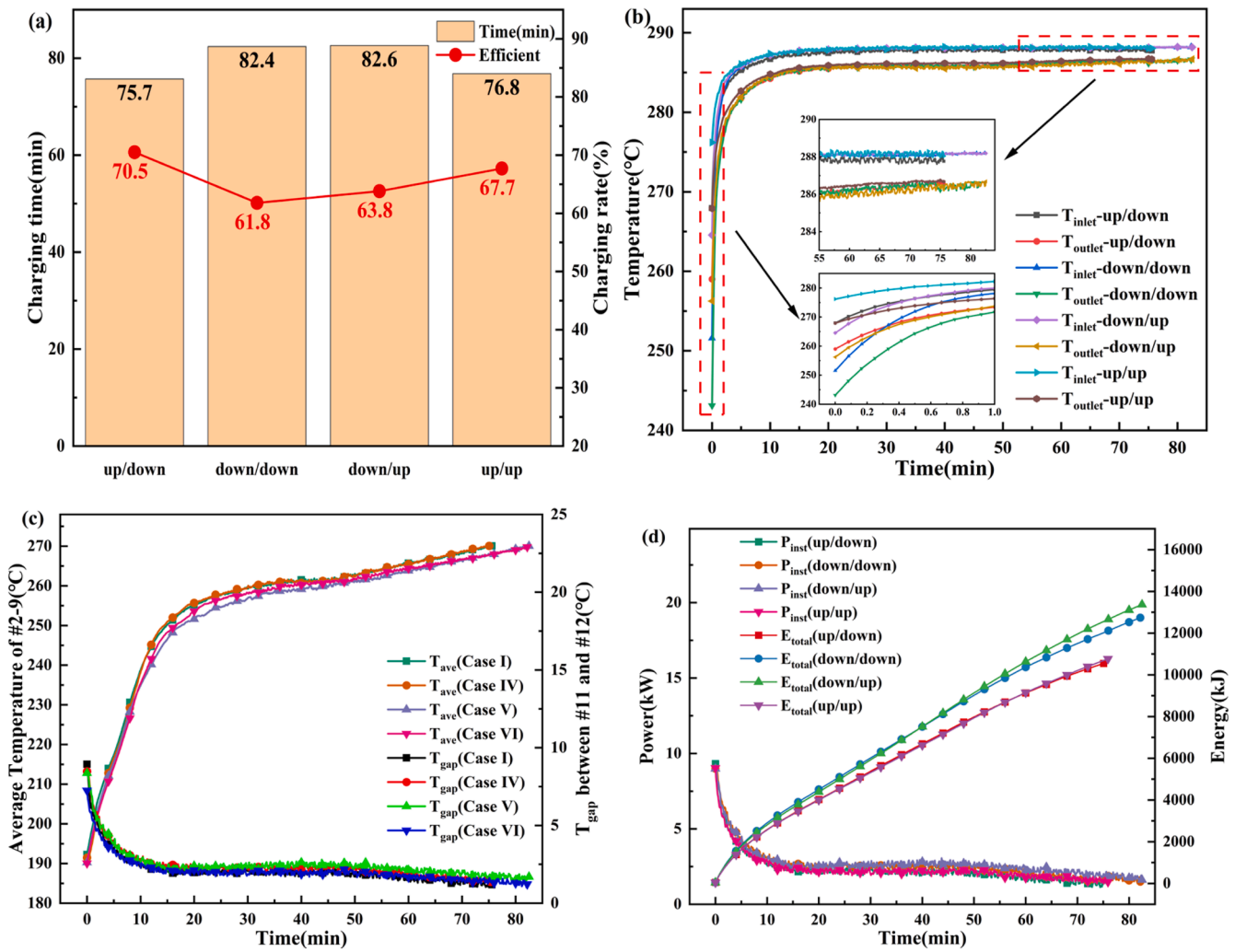

Fig. 14. Plot of variable inlet in charging(a)Time and efficiency(b)Inlet and outlet temperature of HTF(c)Average temperature of PCM and T_{gap} of HTF(d) Instantaneous power and cumulative energy of HTF.

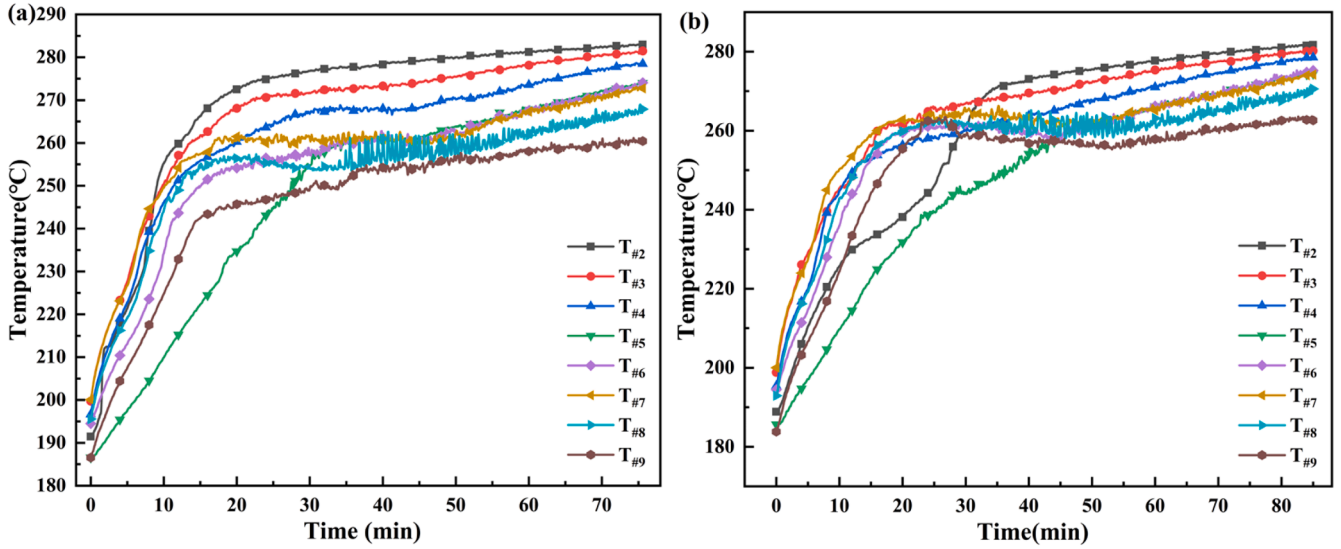

Fig. 15. Plot of #2–9 thermocouple temperature in charging(a) HTF entering from the top (b) HTF entering from the bottom.

preheating temperature reaches 290 °C. The analysis of Fig. 14(c) illustrates that T_{ave} for all four cases exhibits a turning point at 15 min, mirroring the observation discussed in the previous chapter. T_{gap} during charging is relatively high within the first 5 min, approximately 8.5 °C, and then remains relatively stable at 1.5–2 °C. The temperature difference curve corresponds to the power curve in Fig. 14(d), which exhibits similar characteristics, with an initial power of nearly 10 kW, dropping to approximately 2.5 kW after 10 min. The power difference remains relatively stable at around 2.5 kW after 15 min of charging, and the HTF temperature difference and instantaneous power of the two cases where HTF enters from the bottom into TES exhibit slightly higher values by comparison with the other two cases. Since the cumulative energy is calculated by multiplying the instantaneous power and time, two curves appear in the cumulative energy graph.

Fig. 15 shows that the overall temperature curve exhibits a high degree of similarity, suggesting that the varying HTF inlet positions during the charging process have a negligible effect on the central PCM. However, the temperature curves of the #2 and #9 thermocouples near the ends show significant differences. Specifically, the #9 thermocouple temperature rises to 260 °C at 22 min due to the influx of high-temperature HTF. After that, the temperature of #9 remains relatively constant. While the #2 thermocouple temperature presents a "platform" within the 10–30 min range. It is postulated that upon HTF entering TES from the bottom, the heat initiates a phase change in the PCM between the fins first. Once the solid phase is transformed into the liquid phase, the density-reduced liquid PCM flows downwards along the spiral fins to the top, increasing the amount of PCM at the top and strengthening the heat transfer.

Integration of the above data implies that the strict layer-by-layer decrease of PCM's temperature at the end of preheating leads to the conclusion that when HTF enters TES from the bottom, the hot HTF initially exchanges heat with the PCM having the lowest temperature. As HTF flows upwards, its temperature decreases. The temperature of the encountered PCM gradually increases, leading to a slightly higher temperature difference relative to the scenario where HTF enters from the top. Fig. 16 illustrates that the melting of PCM occurs from top to bottom, and based on the material properties described earlier, it is known that the thermal conductivity of liquid PCM exceeds that of solid PCM. Therefore, the case where HTF enters from the top can reduce the charging time, and the reduced charging time also reduces the heat dissipation to the environment, resulting in better thermal efficiencies.

4.3. Effect of different inlets on the discharging process

According to the previous data, the discharging process is completed more rapidly than the charging process, and the average time required for HTF during discharging is not significantly different, as shown in Fig. 17(a), with respective values of 48.05 min and 47.75 min. The average discharging efficiencies are 72.8% and 72.1%, respectively, with a difference of only 0.7%.

Fig. 17(b) depicts the temperature curves of T_{inlet} and T_{outlet} for four different experiments, which exhibit a high degree of consistency, especially during the initial 2 min of discharging. The localized zoomed-in image reveals distinct starting temperatures. When combined with the temperature difference curve in Fig. 17(c), it becomes apparent that the temperature difference is consistently similar, owing to the manual opening of the valve and sampler, which introduces latency in data collection. Through the four graphs in Fig. 17, it is clear that, regardless of the discharging time, efficiency, HTF inlet, and outlet temperature, or PCM's temperature of the different height (Fig. 18), there's no discernible difference, indicating that the position of HTF inlet has a negligible effect on discharging. PCM is liquid at the beginning of discharging, and in the process of cooling down the PCM near the finned tubes is firstly transformed into solid state, which increases the thermal resistance, weakening the effect of the flow rate and the inlet position on the heat transfer.

4.3.1. Effect of different inlets on cycle efficiency

The different inlet positions affect the cycle efficiency from Fig. 19, with up/down having the highest cycle efficiency, reaching 58.35%, and down/up having the lowest cycle efficiency, at 44.97%. The energy absorbed by HTF during the discharging process is nearly consistent, with a maximum of 5082.8 kJ and a minimum of 4871.3 kJ, representing a ratio of 1.043. In contrast, the energy released by HTF during charging has a maximum of 10,893.3 kJ and a minimum of 8709.9 kJ, representing a ratio of 1.25. It concludes that the charging process has a deeper impact on the cycle efficiency than the discharging process.

4.4. Effect of graded heating on charging

The instantaneous power of HTF oscillates during the early charging stage, as depicted in Fig. 20(b). However, it's more desirable to acquire stable and safe instantaneous power in applications. Therefore, introducing graded heating is necessary with the specific experimental

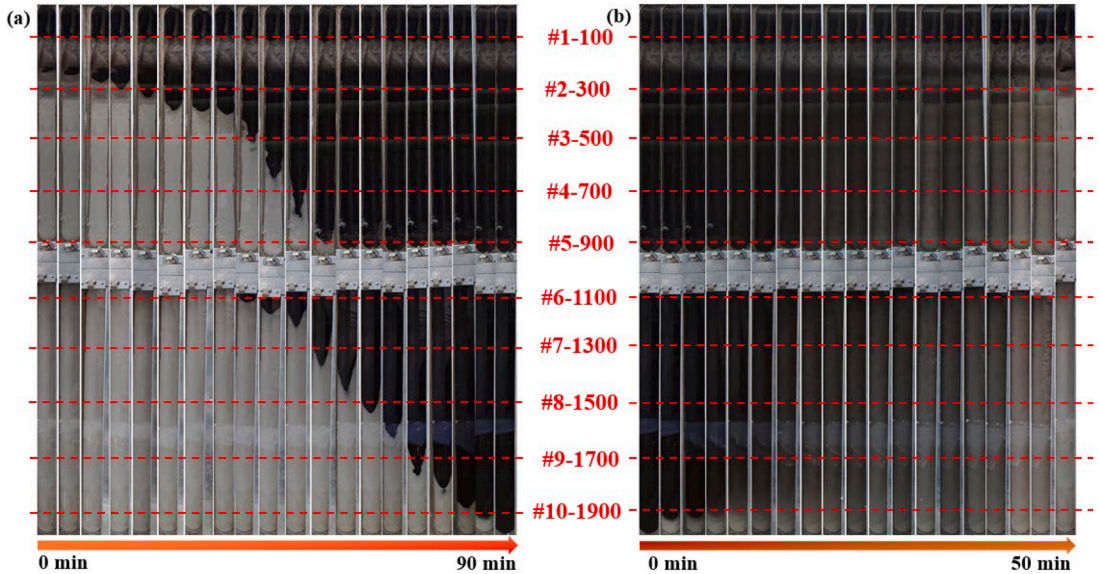

Fig. 16. Graph of PCM over time in(a)charging(b)discharging.

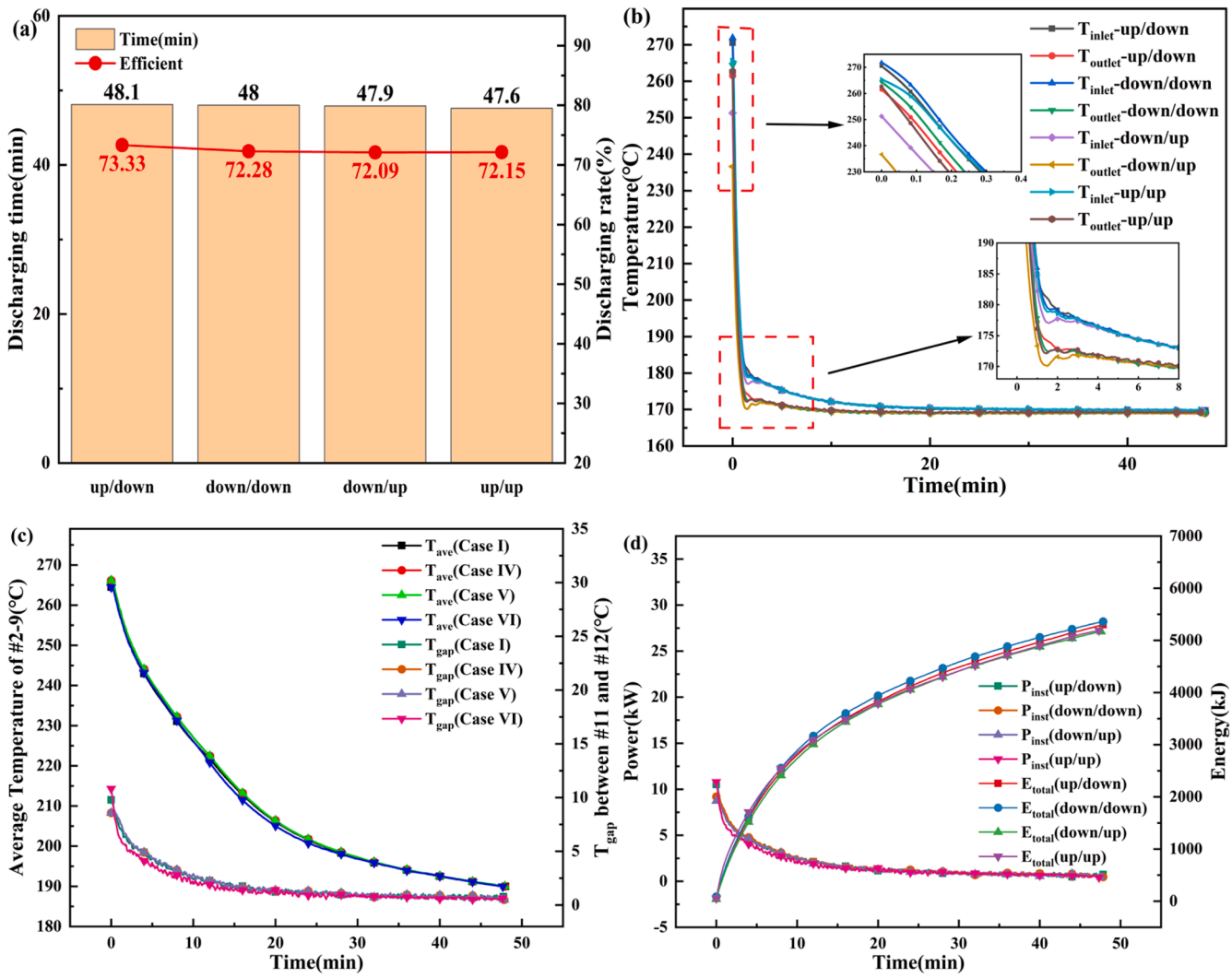

Fig. 17. Plot of variable inlet in discharging(a)Time and efficiency(b)Inlet and outlet temperature of HTF(c)Average temperature of PCM and T_{gap} of HTF(d) Instantaneous power and cumulative energy of HTF.

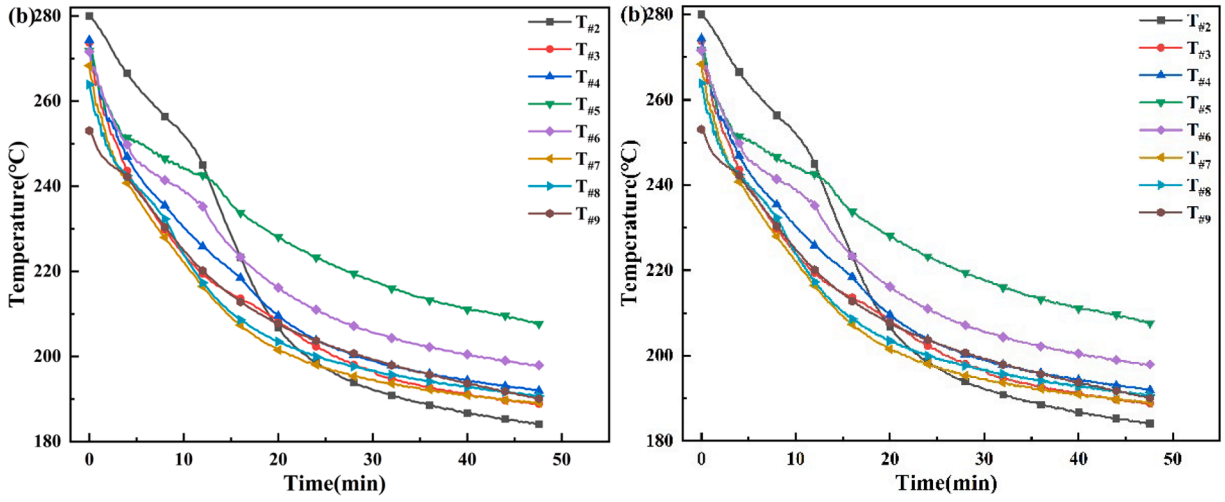

Fig. 18. Plot of #2–9 thermocouple temperature in discharging(a) HTF entering from the top (b) HTF entering from the bottom.

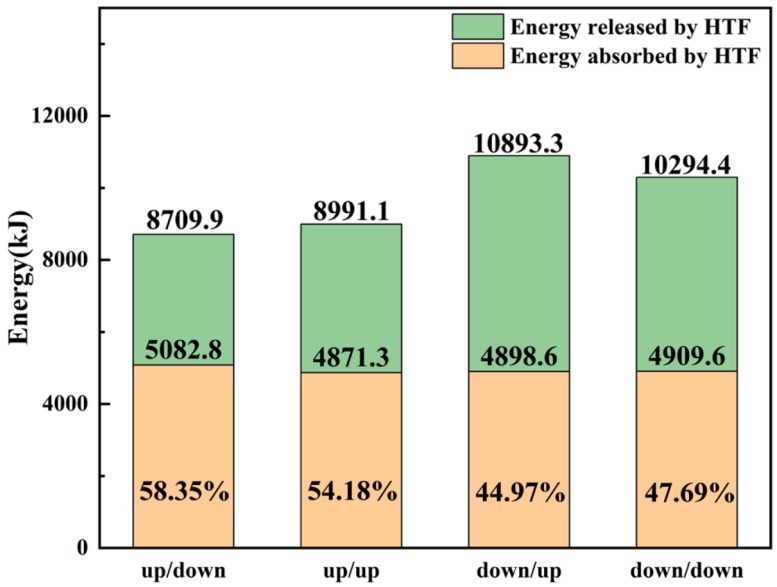

Fig. 19. Plot of cycle efficiency at different conditions.

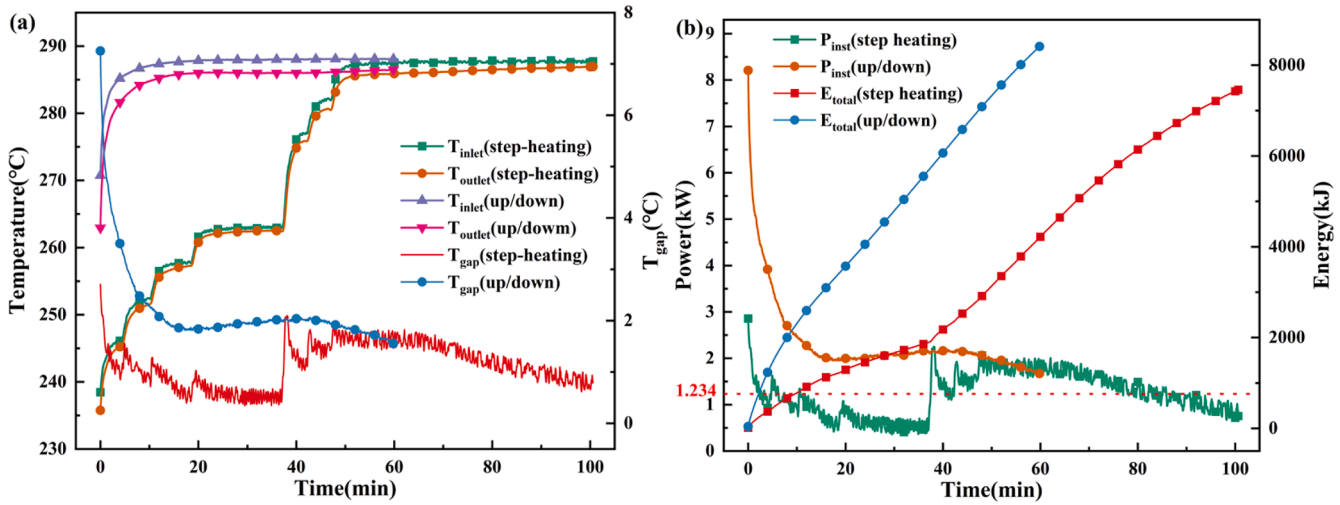

Fig. 20. Graph of comparison between graded heating and constant-temperature heating(a)temperature of HTF inlet/outlet and their difference(b) HTF instantaneous power and accumulated energy.

conditions listed in Table 6.

The HTF inlet and outlet temperatures increase rapidly, reaching approximately 100% of the temperature increase during the initial 10 min of charging. Then, they remain relatively constant for about 50 min. The temperature difference curve gradually decreases from approximately 7 °C to less than 2 °C and then oscillates with a temperature difference of around 2 °C. In contrast, the graded heating curves show the HTF temperature increases rapidly and then gradually stabilizes until the following rise. Graded heating can be subdivided into multiple constant-temperature heating processes. Nevertheless, due to the low gradients of each heating process, the curve of temperature difference shows smaller values. The temperature difference curve shows two distinct crests, corresponding to the initial charging stage and stage 5 in Table 6.

The instantaneous power curve in Fig. 20(b) is similar to the temperature difference curve, with the two peaks of 2.86 kW and 2.25 kW, respectively. According to the data, the average power is 1.234 kW. The instantaneous power of graded heating is generally around the average power, indicating that graded heating can significantly improve the stability of HTF instantaneous power. However, it is also evident that the charging time increases considerably due to the decrease in temperature gradients, which points out the limitations of step-by-step heating.

5. Conclusion

Research on PCM applications in TES has primarily focused on low-temperature experiments or numerical simulations. Therefore, this study employs an experimental approach to investigate a single-tube phase-change heat exchanger at medium and high temperatures. This research has significant implications for the deep integration of LHS with energy networks, guiding the development of strategies to address the disparity between energy generation and consumption. The experiment utilizes a small-scale device, accommodating 33.35 kg of PCM and storing approximately 5.5 MJ of energy. The device features a quartz window on one side, allowing for direct observation of PCM states, which provides a research framework for high-temperature experiments. The following conclusions have been derived through a series of analyses.

(1) The HTF flow rate has a notable influence on both the duration and efficiency of the charging and discharging processes. The increase in HTF flow rate significantly increases the Reynolds number of HTF and the Nusselt number calculated by empirical equations is also enhanced to some extent, resulting in lower heat transfer time and less environmental dissipation. When the HTF flow rate reduces from 33 to 19.8 L/min, the charging time rises by 49.67% and the charging efficiency decreases by 17.96%. Similarly, the discharging time increases by 56.62%, and the discharging efficiency decreases by 6.1%.
(2) The inlet position of HTF affects thermal efficiency, particularly during charging. When HTF enters the TES from the top, the heat storage efficiency is 71.1%, whereas when it enters from the bottom, the efficiency is 62.8%, a decrease of 8.3%. The heat release efficiency is 72.8% and 72.1%, respectively, with a drop of 0.7%.
(3) The system's circulation efficiency increases gradually with increasing HTF flow rate, and HTF entering from the top exhibits better heat transfer performance. During charging, the output energy of HTF is 11,390.4, 10,053.3, and 9335.7 kJ, with relative uncertainties of 1.38%, 1.91%, and 2.46%, respectively. The corresponding circulation efficiencies are 43.45%, 49.32%, and 56.36%.
(4) Graded heating stabilize the instantaneous power during charging by reducing the temperature gradient in each time period, although it increases the charging time by 58.74%. The average value of HTF's instantaneous power is 1.234 kW, with a maximum value of 2.86 kW, much lower than the constant-temperature charging process of 8.34 kW.

CRediT authorship contribution statement

Lei Zhang: Writing – review & editing, Writing – original draft, Investigation, Conceptualization. **Kelang Jin:** Writing – original draft, Methodology, Investigation. **Laiquan Lv:** Writing – review & editing, Methodology, Investigation. **Shengyao Huang:** Writing – review & editing, Writing – original draft. **Xue Xue:** Writing – review & editing, Writing – original draft. **Xiang Liu:** Writing – original draft, Conceptualization. **Hao Zhou:** Supervision, Resources, Methodology, Conceptualization.

Declaration of competing interest

The authors declare that they have no known competing financial interests or personal relationships that could have appeared to influence the work reported in this paper.

Acknowledgments

This work was supported by the Fundamental Research Funds for the Central Universities (2022ZFJH04).

Data availability

Data will be made available on request.

References

[1] BP Energy Outlook:2023 edition. BP Amoco. 2024.
[2] Global Renewables Outlook:Energy transformation 2050, International Renewable Energy Agency, Abu Dhabi, 2020.
[3] Waseem Aftab, Ali Usman, Jinming Shi, Kunjie Yuan, Mulin Qin, Ruqiang Zou, Phase change material-integrated latent heat storage systems for sustainable energy solutions, Energy Environ. Sci. 14 (8) (2021) 4268–4291.
[4] Rhys Jacob, Maximilian Hoffmann, Jann Michael Weinand, Jochen Linßen, Detlef Stolten, Michael Müller, The future role of thermal energy storage in 100% renewable electricity systems, Renew. Sustain. Energy Trans. 4 (2023) 100059.
[5] Hongbo Ren, Zipei Jiang, Qiong Wu, Qifen Li, Yongwen Yang, Integrated optimization of a regional integrated energy system with thermal energy storage considering both resilience and reliability, Energy 261 (2022) 125333.
[6] Y.B. Tao, Ya-Ling He, A review of phase change material and performance enhancement method for latent heat storage system, Renew. Sustain. Energy Rev. 93 (2018) 245–259.
[7] Jasim M. Mahdi, Sina Lohrasbi, Emmanuel C. Nsofor, Hybrid heat transfer enhancement for latent-heat thermal energy storage systems: a review, Int. J. Heat. Mass Transf. 137 (2019) 630–649.
[8] Alessandro Ribezzo, Gabriele Falciani, Luca Bergamasco, Matteo Fasano, Eliodoro Chiavazzo, An overview on the use of additives and preparation procedure in phase change materials for thermal energy storage with a focus on long term applications, J. Energy Storage 53 (2022) 105140.
[9] Ayad K. Hassan, Jasim Abdulateef, Mustafa S. Mahdi, Ahmed F. Hasan. Experimental evaluation of thermal performance of two different finned latent heat storage systems. Case Stud. Therm. Eng.. 2020. 21. 100675.
[10] Xiaohu Yang, Junfei Guo, Bo Yang, Haonan Cheng, Pan Wei, Ya-Ling He, Design of non-uniformly distributed annular fins for a shell-and-tube thermal energy storage unit, Appl. Energy 279 (2020) 115772.
[11] A. Rozenfeld, Y. Kozak, T. Rozenfeld, G. Ziskind, Experimental demonstration, modeling and analysis of a novel latent-heat thermal energy storage unit with a helical fin, Int. J. Heat. Mass Transf. 110 (2017) 692–709.
[12] Saeed Tiari, Addison Hockins, Kyle Shank, Experimental study of a latent heat thermal energy storage system assisted by varying annular fins, J. Energy Storage 55 (2022) 105603.
[13] Ramin Karami, Babak Kamkari, Experimental investigation of the effect of perforated fins on thermal performance enhancement of vertical shell and tube latent heat energy storage systems, Energy Convers. Manage 210 (2020) 112679.
[14] Yuanhao Wu, Hayder I. Mohammed, Sheng Chen, Maji Luo, Yang Yu, Zijian Zhou, Numerical investigation of the impact of toothed fins on the heat transfer performance of a shell-and-tube exchanger during phase change material melting process, Int. J. Heat. Mass Transf. 217 (2023) 124637.
[15] Abdullah Bahlekeh, Hosseinali Ramezani Mouziraji, Hussein Togun, Abolfazl Ebrahimnataj Tiji, Azher M. Abed, Hayder I. Mohammed, Raed Khalid Ibrahem, Muataz S. Alhassan, Pouyan Talebizadehsardari, Evaluation of the solidification process in a double-tube latent heat storage unit equipped with circular fins with optimum fin spacing, Energy Sci. Eng. 11 (7) (2023) 2552–2570.
[16] Ammar M. Abdulateef, Sohif Mat, Jasim Abdulateef, Kamaruzzaman Sopian, Abduljalil A. Al-Abidi, Geometric and design parameters of fins employed for enhancing thermal energy storage systems: a review, Renew. Sustain. Energy Rev. 82 (2018) 1620–1635.
[17] Nidhal Ben Khedher, Hussein Togun, Azher M. Abed, Hussein M.Taqi Al-Najjar, Anmar Dulaimi, Hayder I. Mohammed, Jasim M. Mahdi, A. Yvaz, Pouyan Talebizadehsardari, Discharge performance assessment of a vertical double-pipe latent heat storage unit equipped with circular Y-shaped fins, J. Build. Eng. 75 (2023) 106870.
[18] A. Shukla, K. Kant, Pascal Henry Biwole, R. Pitchumani, Atul Sharma, Melting and solidification of a phase change material with constructal tree-shaped fins for thermal energy storage, J. Energy Storage 53 (2022) 105158.
[19] Yongxue Zhang, Bohui Lu, Zixi Wang, Jianjun Zhu, Jinya Zhang, Cong Wang, Experimental investigation on the charging and discharging performance enhancement of a vertical latent heat thermal energy storage unit via snowflake fin design, Int. J. Heat. Mass Transf. 199 (2022) 123455.
[20] Yunxiang Chen, Yun Liu, Liang Zeng, Wenxun Cui, Jianfei Xie, A novel topology optimization of fin structure in shell-tube phase change accumulator considering the double objective functions and natural convection, J. Energy Storage 80 (2024) 110327.
[21] P. Zhang, F. Ma, X. Xiao, Thermal energy storage and retrieval characteristics of a molten-salt latent heat thermal energy storage system, Appl. Energy 173 (2016) 255–271.
[22] Pouyan Talebizadeh Sardari, Hayder I. Mohammed, Donald Giddings, Gavin S. Walker, Mark Gillott, David Grant, Numerical study of a multiple-segment metal foam-PCM latent heat storage unit: effect of porosity, pore density and location of heat source, Energy 189 (2019) 116108.
[23] Mohammad Parsazadeh, Xili Duan, Numerical study on the effects of fins and nanoparticles in a shell and tube phase change thermal energy storage unit, Appl. Energy 216 (2018) 142–156.
[24] S. Jegadheeswaran, Sanjay D. Pohekar, Performance enhancement in latent heat thermal storage system: a review, Renew. Sustain. Energy Rev. 13 (9) (2009) 2225–2244.
[25] Yongcai Huang, Alex Stonehouse, Chamil Abeykoon, Encapsulation methods for phase change materials – A critical review, Int. J. Heat. Mass Transf. 200 (2023) 123458.
[26] Gerard Peiró, Jaume Gasia, Laia Miró, Luisa F. Cabeza, Experimental evaluation at pilot plant scale of multiple PCMs (cascaded) vs. single PCM configuration for thermal energy storage, Renew. Energy 83 (2015) 729–736.
[27] Mohamed Fadl, Philip C. Eames, An experimental investigation of the heat transfer and energy storage characteristics of a compact latent heat thermal energy storage system for domestic hot water applications, Energy 188 (2019) 116083.
[28] Sandip Khobragade, Jaya Krishna Devanuri, Thermal analysis of latent heat storage system in vertical and horizontal configurations under simultaneous charging and discharging processes, Therm. Sci. Eng. Progress 36 (2022) 101479.
[29] Sandip Khobragade, Jaya Krishna Devanuri, Impact of inclination on the thermal performance of shell and tube latent heat storage system under simultaneous charging and discharging: numerical investigation, Appl. Therm. Eng. 214 (2022) 118811.

[30] Appolinaire Kaboré, Jules Voguelin Simo Tala, Zohir Younsi, Daniel Bougeard, Natural convection and field synergy principle analysis of the influence of fins redistribution on the performance of a latent heat storage unit in a successive charge and discharge, J. Energy Storage 89 (2024) 111855.
[31] Muhammad Shaban, Talha Irfan Khan, Muhammad Anwar, Meshal Alzaid, Rakan Alanazi, Effect of Asymmetric Fins on Thermal Performance of Phase Change Material-Based Thermal Energy Storage Unit, Materials. (Basel) 16 (7) (2023) 2567.
[32] Rishav Kumar, Prashant Verma, An experimental and numerical study on effect of longitudinal finned tube eccentric configuration on melting behaviour of lauric acid in a horizontal tube-in-shell storage unit, J. Energy Storage 30 (2020) 101396.
[33] Kamel Guedri, Pavitra Singh, Fahid Riaz, Abrar Inayat, Nehad Ali Shah, Bandar M. Fadhl, Basim M. Makhdoum, Akbar Arsalanloo, Solidification acceleration of phase change material in a horizontal latent heat thermal energy storage system by using spiral fins, Case Stud. Therm. Eng. 48 (2023) 103157.
[34] Mohammadreza Ebrahimnataj Tiji, Waleed Khalid Al-Azzawi, Hayder I. Mohammed, Anmar Dulaimi, Farhan Lafta Rashid, Jasim M. Mahdi, Hasan Sh. Majdi, Pouyan Talebizadehsardari, Hafiz Muhammad Ali, Thermal management of the melting process in a latent heat triplex tube storage system using different configurations of frustum tubes, < 2022 (1) (2022).
[35] Zhao Ma, Wei-Wei Yang, Fan Yuan, Bo Jin, Ya-Ling He, Investigation on the thermal performance of a high-temperature latent heat storage system, Appl. Therm. Eng. 122 (2017) 579–592.
[36] P. Zhang, F. Ma, X. Xiao, Thermal energy storage and retrieval characteristics of a molten-salt latent heat thermal energy storage system, Appl. Energy 173 (2016) 255–271.
[37] Laiquan Lv, Yang Zou, Shengyao Huang, Xinyi Wang, Rongyu Shao, Xue Xue, Yan Rong, Hao Zhou, Experimental study on a pilot-scale medium-temperature latent heat storage system with various fins, Renew. Energy 205 (2023) 499–508.
[38] Laiquan Lv, Shengyao Huang, Yang Zou, Xinyi Wang, Hao Zhou, Heat transfer and thermal resistance analysis under various heat transfer fluid flow rates based on a medium-temperature pilot-scale latent heat storage system, Int. J. Heat. Mass Transf. 220 (2024) 124896.
[39] S.J. Kline, F.A. Mcclintock, Describing uncertainties in single-sample experiments, Mech. Eng. (New York, N.Y.: 1919) 75 (1) (1953).